Soil Dynamics and Earthquake Engineering 39 (2012) 128–137

Contents lists available at SciVerse ScienceDirect

Soil Dynamics and Earthquake Engineering

journal homepage: www.elsevier.com/locate/soildyn

Estimate of shear wave velocity, and its time-lapse change, from seismic data recorded at the SMNH01 station of KiK-net using seismic interferometry

Andrés Pech [a,*], Francisco J. Sánchez-Sesma [b], Roel Snieder [c], Filiberto Ignacio-Caballero [a], Alejandro Rodríguez-Castellanos [d], José Carlos Ortíz-Alemán [d]

[a] Centro Interdisciplinario de Investigación para el Desarrollo Integral Regional, Instituto Politécnico Nacional, Hornos 1003, Santa Cruz Xoxocotlán, Oaxaca, México
[b] Instituto de Ingeniería, Universidad Nacional Autónoma de México, Cd. Universitaria 3000, Circuito Escolar s/n, Coyoacán 04510, Distrito Federal, México
[c] Center for Wave Phenomena, Colorado School of Mines, 1500 Illinois Street, Golden, Colorado, USA
[d] Instituto Mexicano del Petróleo, Eje Central Lázaro Cárdenas Norte 152, Distrito Federal, México

ARTICLE INFO

Article history:
Received 13 September 2011
Received in revised form
5 February 2012
Accepted 19 March 2012
Available online 6 April 2012

ABSTRACT

This study uses the deconvolution of small earthquakes registered in the SMNH01 station of KiK-net, one of the most important seismic networks which is located in Japan, to estimate effective shear wave velocities β, shear modulus μ, and quality factors Q, and to identify physical changes in the soil. This station has a borehole which is equipped with triaxial accelerometers installed at the surface and at 100 m of depth. By deconvolving seismic events registered at surface and at 100 m of depth, we obtain physical parameters. To interpret deconvolved waves, we use a one dimensional (1D) layered medium. Based on changes observed in amplitudes and arrival times of deconvolved waves, we identify time-lapse variations in shear wave velocities (maximum change in $\delta\beta/\beta=3.8\%$) and shear modulus (maximum change in $\delta\mu/\mu=7.8\%$). The variations in shear wave velocities detected at station SMNH01 are mainly due to the combined influence of precipitation and recurrent seismic events.

1. Introduction

The aim of this paper is to use seismic interferometry based on deconvolution to obtain effective shear wave velocities (β), shear modulus (μ), and quality factors (Q) from seismic events recorded by KiK-net, one of the most important seismic networks which is located in Japan, and to identify changes in the soil from the estimated properties. The estimation of near-surface physical properties must be carried out using extremely sensitive tools in order to detect small variations in physical properties. Seismic interferometry is a powerful new technique employed in monitoring materials and structures. It allows for the characterization of materials and structures through correlation and deconvolution of signals [1–10].

Deconvolution has been successfully utilized in a variety of fields. In earthquake engineering, Trampert et al. [11] employed deconvolution to estimate quality factors from borehole seismic data. In addition they were able to obtain the attenuation operator for layered media using an *SH* wave propagator matrix. Mehta et al. [12] estimated the *S* and *P* wave velocities corresponding to a soil composed of layers of sand, and deduced these velocities by deconvolving seismic events registered in boreholes. Deconvolution has also been used to study time-lapse changes in seismic velocities caused by strong earthquakes in shallow ground. For instance, Sawazaki et al. [13] found time-lapse changes of seismic velocities generated by the 2000 Tottori earthquake. They observed an almost complete shear modulus recovery over a period of one year. Rubinstein and Beroza [14] identified changes in *S*-wave velocities produced by strong earthquakes by measuring the *S*-wave traveltimes of repeating earthquakes and detecting delays in traveltimes at the stations where the 1989 Loma-Prieta earthquake was recorded. Rubinstein and Beroza [15] studied changes in *S*-wave traveltimes after the 2004 Parkfield earthquake. Their study shows that the major changes in *S*-wave velocity caused by strong earthquakes occur in shallow ground.

An extensive recent study applied the deconvolution method to a strong motion data set recorded at the surface and in boreholes in northeast Honshu, Japan, to characterize the nonlinear effects of the soil in that location during strong shaking, and to show both the change in the subsurface velocity profile during the movement and the recovery of near-surface physical properties [16].

In the present investigation, we utilize small earthquakes recorded at the SMNH01 station of KiK-net to obtain soil physical properties and to identify time-lapse changes in arrival times and amplitudes of deconvolved waves. This station is located in an

* Corresponding author. Tel./fax: +52 951 517 0610.
E-mail address: apech@ipn.mx (A. Pech).

0267-7261/$ - see front matter © 2012 Elsevier Ltd. All rights reserved.
http://dx.doi.org/10.1016/j.soildyn.2012.03.009

area composed of sand and gravel overlying basalt and has a borehole equipped with two triaxial accelerometers which are installed on the ground and at 100 m of depth. The sensor deployed at 100 m is settled in solid rock, which in this case is basalt. We deconvolve the east–west records using the horizontal movement detected at surface. In order to interpret the deconvolved data, we employ a model constituted of elastic layers overlying an elastic half-space. We consider only the vertical incidence of *SH* waves. This model makes it possible to theoretically derive the main characteristics of the deconvolved fields. This derivation is similar to that of [11] in the sense that we use a 1D layered medium. However, instead of using a propagator matrix for *SH* waves, we represent explicitly the displacement fields, allowing us to directly obtain theoretical deconvolutions. From the small seismic events, we identify changes in the arrival times and amplitudes of deconvolved shear waves. In particular, the variations observed in the amplitude and arrival time of the main ascending and descending waves corresponding to the first and final deconvolved arrivals detected by the deepest receiver make it possible to infer changes in near-surface physical properties. We also observe strong amplitude decay in the deconvolved traces. In contrast to the behavior of the sediments surrounding the SMNH01 station, the sediments of the Valley of Mexico, composed mainly of clays, may produce significant attenuation, but continue to behave linearly, even in the presence of strong shaking (e.g. deconvolved arrivals do not show any important change in amplitude and arrival time), as Singh et al. [17] concluded in their analysis of strong motion data in Mexico City after the September 19th, 1985, Ms 8.1 Michoacan earthquake. We utilize the effective shear wave velocities obtained from the seismic events recorded at the SMNH01 station to illustrate changes in near-surface properties.

This paper is organized in the following manner: in Section 2, we describe the study site and seismic data; in Section 3, we show and describe the deconvolved data; in Section 4, we introduce the mathematical model; in Section 5, we introduce the theoretical deconvolutions and interpret the deconvolved data; in Section 6, we define the expressions that relate variations in near-surface properties with amplitudes and arrival times of deconvolved waves; in Section 7, we present the discussions; in Section 8, we show the conclusions; and in the Appendix A, we derive the attenuation operator for layered media using explicit expressions for the displacement fields.

2. Seismic data recorded by KiK-net

KiK-net is composed of 700 stations distributed across Japan [18]. In this study, we used the east–west (EW) horizontal component of seismic events recorded at the SMNH01 station, which forms part of this network, to estimate physical properties. In Fig. 1, the SMNH01 station is marked with a triangle; the epicenters of the earthquakes utilized in our study are identified with diamonds. The sediments at this station have contributed to the large amplifications and long durations observed in seismic events recorded at this location. In addition, these sediments have experienced physical changes which are mainly due to earthquakes [13].

The SMNH01 station is equipped with two accelerometers which are deployed at surface and at 100 m of depth. The sampling interval for all KiK-net stations is 0.01 s. The subsurface materials reported for this area are sand with gravel for the first 13.5 m, and only basalt below 13.5 m. According to the well-logging data shown in Fig. 2, the *S*-wave velocities at this station range from 290–2800 m/s. Table 1 shows the main characteristics of the earthquakes used to estimate the seismic response at the SMNH01 station.

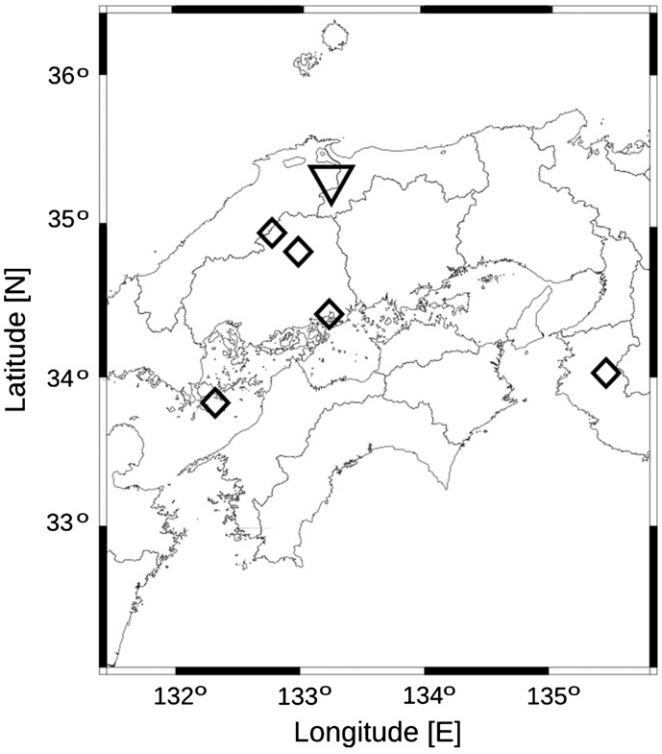

Fig. 1. SMNH01 station (triangle) and epicenter coordinates (diamonds).

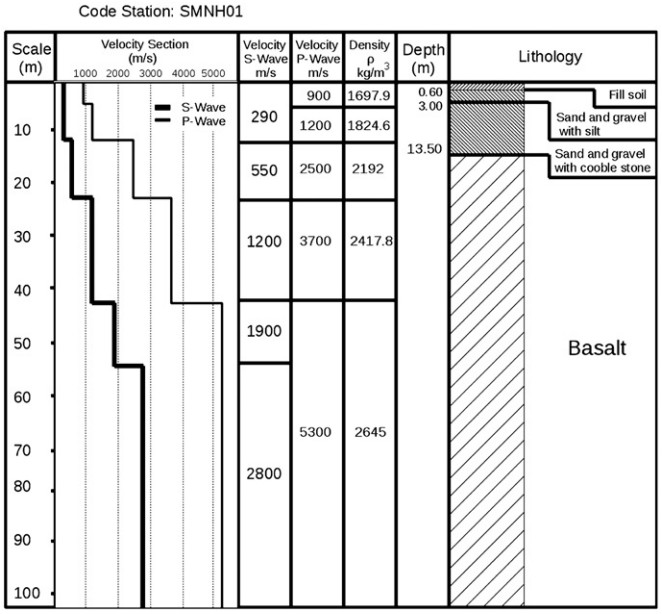

Fig. 2. Wave velocities, density profile, and lithology for the SMNH01 station. The density ρ was obtained using the equation $\rho=310\alpha^{(0.25)}$ [13].

Fig. 3 shows three seismic events registered at the surface that correspond to EW components of the following earthquakes (time breaks are referred to GMT): a seismic event that occurred on 16/07/99 at 02:59 (Fig. 3a), an earthquake that happened on 21/01/10 at 08:50 (Fig. 3b), and a seismic event that occurred on 07/02/11 at 00:36 (Fig. 3c). The rectangle in each accelerogram indicates the *S*-wave arrival used for the deconvolutions.

3. Deconvolved data

In order to estimate the seismic response at the SMNH01 station from seismic events recorded by the vertical array of sensors installed at this site, we select time windows, taking into account the time interval corresponding to *S*-waves in the EW horizontal components. To set the origin of each trace equal to zero, we remove the DC component of the data by subtracting the average of each seismogram [19]. We process the selected windows in the frequency domain, and apply the fast Fourier transform (FFT) to the selected intervals. Given that the accelerograms contain noise, we filter the time windows before deconvolution by applying a band pass filter; the corner frequencies of this filter are 1 and 13 Hz [19]. We select 13 Hz to eliminate high frequency noise. We then deconvolve the filtered windows for each seismic event using the corresponding movement detected at the surface. Finally, we transform the deconvolved windows to the time domain using the inverse fast Fourier transform (IFFT). The following equation is used to perform deconvolution [20]:

$$R(\omega) = \frac{A(\omega)B^*(\omega)}{\phi(\omega)}F(\omega), \quad (1)$$

where $B^*(\omega)$ represents the conjugate of the Fourier transform of the signal $b(t)$, $\phi(\omega) = \max(B(\omega)B^*(\omega), \varepsilon\ |B|^2_{max})$, ε is a "water level" parameter which helps to manage the instabilities of the ratio (in all the examples $\varepsilon = 0.0001$, we select this value, because we find empirically that this is the smallest regularization parameter to get stable waveforms), $F(t) = \zeta\exp(-\omega^2/(4m^2))$, ζ is a normalization factor, and m is the width of the Gaussian filter (in all the examples, $m = 100$ Hz). In the above equation, the product of $A(\omega)B^*(\omega)$ defines in the frequency domain the correlation of the signals $a(t)$ and $b(t)$.

To calculate shear wave velocities, we first obtain arrival times by selecting the times associated with the peaks of the main ascending and descending deconvolved waves [12] (at this step, we use quadratic interpolation to define the arrival times with better accuracy, interpolation enhances time resolution [19]). These arrival times are then averaged. Given that we know the depths of the receivers, we compute the propagation velocities by dividing receiver distance over the averaged arrival times. Table 2 displays the effective shear wave velocities and shear modulus estimated from seismic events detected by the vertical array of sensors deployed at the SMNH01 station. In this table, β indicates the effective *S*-wave velocity that we obtained by deconvolving the motion recorded at 100 m with the corresponding movement registered at surface, μ denotes the respective shear modulus.

Table 1
Data corresponding to the earthquakes used in this study.

Date	Magnitude (M_W)	Latitude	Longitude	Depth (km)	Epicentral distance (km)
16/07/99	4.4	34.417	133.200	20	97
21/08/99	5.4	34.050	135.467	70	245
21/01/10	3.4	34.982	132.816	8	53
21/02/10	4.5	33.822	132.310	13	185
07/02/11	3.6	34.889	133.028	9	50

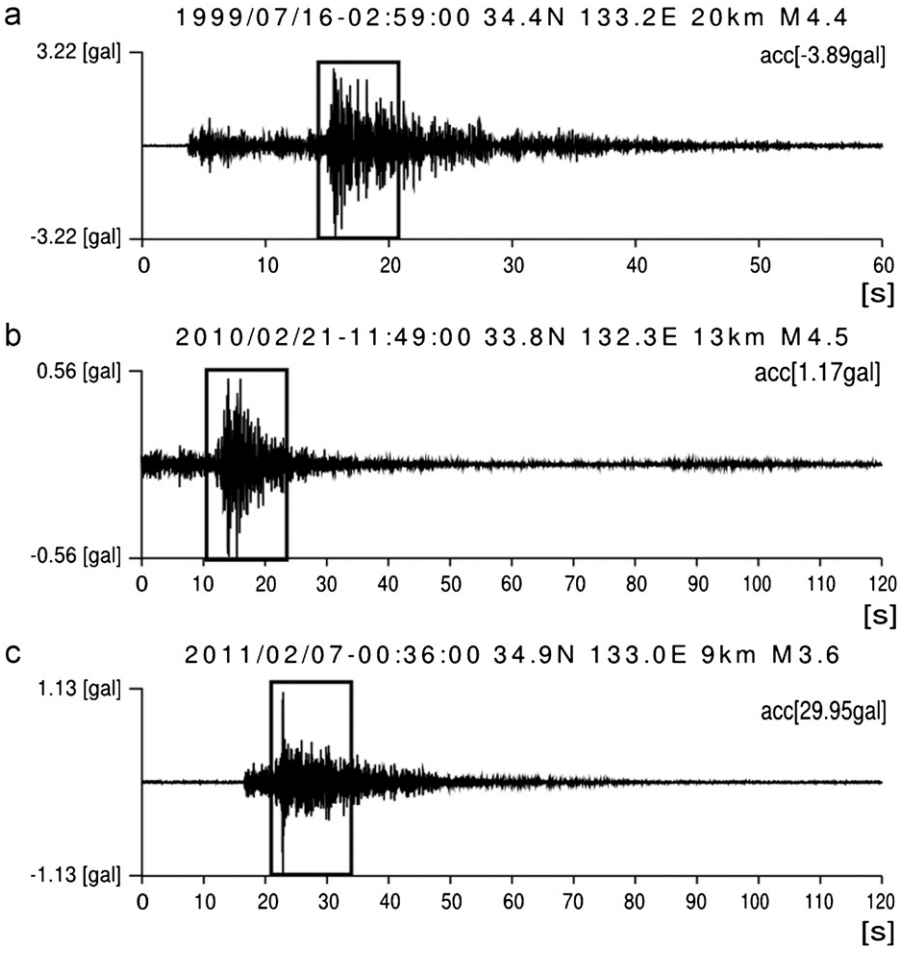

Fig. 3. Seismic events recorded at the surface at the SMNH01 station.

Table 2
Physical parameters estimated from deconvolved events. The shear modulus μ was obtained using $\mu=\rho\beta^2$. The density ρ was calculated from $\rho=310\alpha^{(0.25)}$ [11]. The *P*-wave velocity α was obtained by deconvolving vertical components containing the movement induced by *P*-waves.

Date	β (m/s)	μ (MPa)	Q	
			Sediments	Basalt
16/07/99	1242.2	3892.7	–	–
21/08/99	1273.9	4093.9	12	200
21/01/10	1290.3	4200	–	–
21/02/10	1265.8	4042	–	–
07/02/11	1290.3	4200	–	–

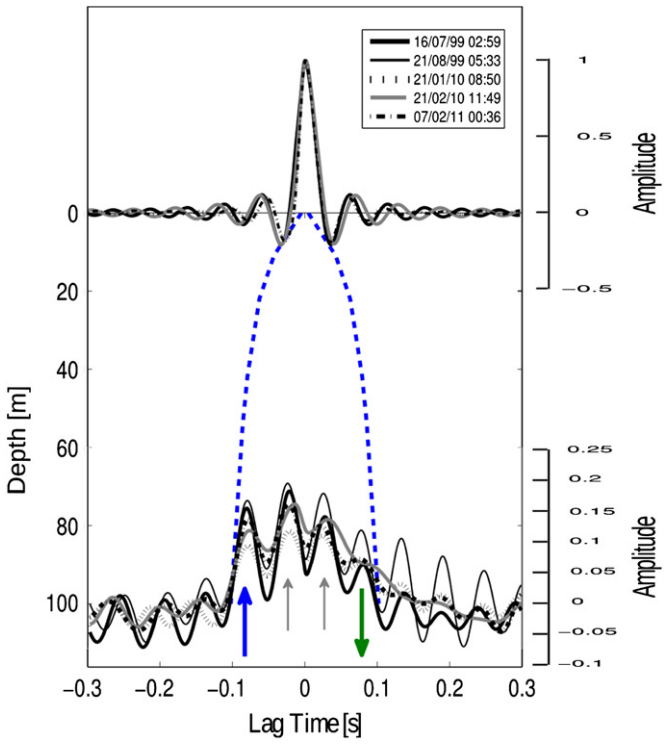

Fig. 4. Deconvolved traces corresponding to the seismic events listed in Table 1.

Table 2 also displays two quality factors *Q*, which were obtained by fitting synthetic deconvolved data to real deconvolutions.

Fig. 4 shows deconvolved time waveforms corresponding to the following events (time breaks are referred to GMT): a seismic event that occurred on 16/07/99 at 02:59 (thick black line), an earthquake that happened on 21/08/99 at 05:33 (thin black line), an earthquake that occurred on 21/02/10 at 11:49 (thin gray line), an event that happened on 21/01/10 at 08:50 (black dotted line), and an earthquake that occurred on 07/02/2011 at 00:36 (black dashed-and-dotted line). This figure also displays the *S*-wave traveltimes obtained from well-logging data in thick dashed blue lines. The variations in the slopes of the thick dashed blue lines denote subtle changes in *S*-wave propagation velocity. In general, logging data and travel times detected from seismic waves are not completely identical since they are measuring slightly different properties. The discrepancy came from a variety of factors, such as the uncertainty of the logging velocities, the measuring method, the wavelength, and time-lapse changes.

In Fig. 4, we indicate the "main" arrivals with thick arrows. These arrivals correspond to ascending (thick blue upward-pointing arrow) and descending waves (thick green downward-pointing arrow). There is a good agreement between the traveltimes shown in thick dashed blue lines and the traveltimes associated with the arrivals denoted by the thick arrows. They are not equal as a result of the known differences mentioned above.

Fig. 4 has several important features, described below:

- The amplitudes of the waves denoted by the thick green downward-pointing arrow are smaller than those of the waves indicated by the thick blue upward-pointing arrow.
- The amplitudes of the waves indicated with thin gray arrows are not negligible.
- The amplitudes of the main ascending arrivals (denoted by the thick blue upward-pointing arrow) are smaller than the amplitudes of the corresponding band-limited Dirac delta functions observed in the deconvolved traces associated with the surface.
- There is a high variability in terms of deconvolved amplitudes.

We interpret these characteristics in the following sections.

4. A stratified medium under incidence of plane *SH* waves

In this section, we briefly review the equations used to represent displacement fields. We utilize a model that contains elastic homogeneous isotropic layers, as Fig. 5 illustrates. At $z=0$, there is a free-stress boundary condition. Between any pair of layers, displacements and tractions are continuous. This is also true for the contact defined by the last layer and the half-space. We only consider the propagation of *SH* plane waves along the *z* axis. In the particular case studied here, *SH* waves generate a particle motion perpendicular to the plane *xz*. Various authors have utilized the layered medium shown in Fig. 5 to study the seismic response of alluvial valleys [21–27]. The general equations that govern displacements in the stratified medium illustrated in Fig. 5 are defined below:

$$U_1 = A_1 e^{i\omega t} e^{ik_1 z} + A_2 e^{i\omega t} e^{-ik_1 z} \quad (2)$$

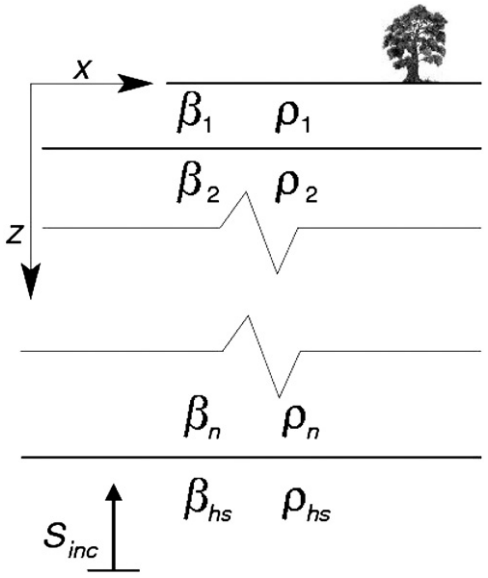

Fig. 5. Stratified medium containing *n* layers overlying a half-space; ρ_1, ρ_2, ρ_n, and ρ_{hs} denote densities of the first, second, and *n* layer and half-space, respectively; β_1, β_2, β_n, and β_{hs} denote shear wave velocities of the first, second, and *n* layer and half-space, respectively; S_{inc} represents the incident wave.

$$U_n = A_{2n-1}e^{i\omega t}e^{ik_n z} + A_{2n}e^{i\omega t}e^{-ik_n z}, \quad (3)$$

$$U_{hs} = A_0 e^{i\omega t}e^{ik_{hs} z} + A_{2n+1}e^{i\omega t}e^{-ik_{hs} z}, \quad (4)$$

where A_0=amplitude of the incident wave; t=time; ω=angular frequency; z=depth; $i=\sqrt{-1}$; U_1, U_n, and U_{hs} are the *SH* displacements corresponding to the first layer, n layer, and half-space; $A_1, A_2, \ldots, A_{2n-1}, A_{2n}$, and A_{2n+1}=amplitudes of the ascending and descending waves which travel through the model (the boundary conditions used to obtain these coefficients are $\mu_1 \partial U_1/\partial z|_{z=0} = 0$, free stress boundary condition, and $U_n = U_{n+1}$ and $\mu_n \partial U_n/\partial z = \mu_{n+1}\partial U_{n+1}/\partial z$, elastic boundary conditions, where $\mu = \rho\beta^2$, ρ is the density and β is the shear wave velocity); and k_1, k_n, and k_{hs}=the wave numbers corresponding to the first layer, n layer, and half-space.

5. Theoretical deconvolutions for a layered medium

In this section, we illustrate the behavior of deconvolved fields using theoretical displacements measured in layered media. For the sake of simplicity, we use the layered medium illustrated in Fig. 6. We calculate the displacement fields at three different positions. In this case, $U_1(a,\omega)$, $U_2(h_1+b,\omega)$, and $U_3(h_1+h_2+c,\omega)$ represent the displacements corresponding to depths a, h_1+b, and h_1+h_2+c. $U_1(0,\omega)$ denotes the displacement at surface level. By deconvolving the movement recorded at any given depth within the first layer with the motion detected at surface, we obtain

$$\frac{U_1(a,\omega)}{U_1(0,\omega)} = \frac{1}{2}e^{-ik_1 a} + \frac{1}{2}e^{ik_1 a}. \quad (5)$$

We use the free stress boundary condition described in the previous section to obtain the amplitudes of the two waves defined in the previous equation, such amplitudes are identical and equal to 1/2. Assuming for the moment that there is no attenuation and applying the inverse Fourier transform to the previous equation (considering here and hereafter that $\int_{-\infty}^{\infty}\delta(t-\tau)e^{-i\omega t}dt = e^{-i\omega\tau}$) gives

$$\frac{u_1(a,t)}{u_1(0,t)} = \frac{1}{2}\overbrace{\delta\left(t+\frac{a}{\beta_1}\right)}^{1} + \frac{1}{2}\overbrace{\delta\left(t-\frac{a}{\beta_1}\right)}^{2} \quad (6)$$

From the structure of the previous equation, we can establish that when $z=a$, two arrivals are observed, corresponding to waves 1 (up-going) and 2 (down-going). The amplitude of both arrivals is 1/2.

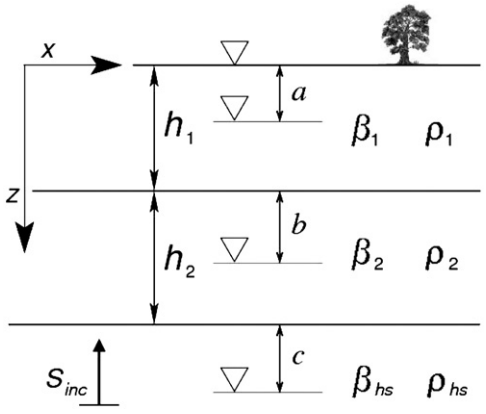

Fig. 6. Coordinates of the array of receivers where the equations that govern the displacement fields were evaluated; ρ_1, ρ_2, and ρ_3 denote densities of the first, second, and third layer, respectively; β_1, β_2, and β_3 denote shear wave velocities of the first, second, and third layer, respectively; S_{inc} represents the incident wave. h_1 and h_2 denote the thickness of the first and second layer, respectively. ρ_{hs} and β_{hs} indicate the density and velocity of the half-space, respectively.

We can infer from this equation that at $z=0$, these waves interfere constructively, producing only one arrival with unitary amplitude. Eq. (5) is equivalent to Eq. (3) of Trampert et al. [11]. By deconvolving $U_2(h_1+b,\omega)$ with the surface displacement, we get

$$\frac{U_2(h_1+b,\omega)}{U_1(0,\omega)} = \frac{k_2\beta_2^2\rho_2 + k_1\beta_1^2\rho_1}{4k_2\beta_2^2\rho_2}\left(e^{i(-k_1h_1-k_2b)} + e^{i(k_1h_1+k_2b)}\right) + \frac{k_2\beta_2^2\rho_2 - k_1\beta_1^2\rho_1}{4k_2\beta_2^2\rho_2}\left(e^{i(-k_1h_1+k_2b)} + e^{i(k_1h_1-k_2b)}\right) \quad (7)$$

This equation denotes contrasts in velocity, density and absorption. In addition, if, for instance, in the first layer the quality factor Q_1 is frequency dependent, the amplitudes in the right hand side, as expressed in (7), also depend on frequency. Assuming that for the moment there is no attenuation and transforming Eq. (7) to the time domain gives

$$\frac{u_2(h_1+b,t)}{u_1(0,t)} = \frac{1}{2T_1}\left[\overbrace{\delta\left(t+\frac{h_1}{\beta_1}+\frac{b}{\beta_2}\right)}^{3} + \overbrace{\delta\left(t-\frac{h_1}{\beta_1}-\frac{b}{\beta_2}\right)}^{4}\right] + \frac{R_1}{2T_1}\left[\overbrace{\delta\left(t+\frac{h_1}{\beta_1}-\frac{b}{\beta_2}\right)}^{5} + \overbrace{\delta\left(t-\frac{h_1}{\beta_1}+\frac{b}{\beta_2}\right)}^{6}\right] \quad (8)$$

where $R_1 = (\beta_2\rho_2 - \beta_1\rho_1)/(\beta_2\rho_2 + \beta_1\rho_1)$ and $T_1 = (2\beta_2\rho_2)/(\beta_2\rho_2 + \beta_1\rho_1)$. The simplicity of this equation facilitates the analysis of the deconvolved fields. The first term of the right hand side is made up of two waves, one ascending and the other descending (waves 3 and 4, respectively). These waves have the same amplitude, defined by the factor $1/(2T_1)$. The second term of Eq. (8) also contains two waves, but with amplitudes equal to $R_1/2T_1$. Since $(1/2T_1) > (R_1/2T_1)$, the waves in the second term are weaker than those in the first term. It is clear that waves 5 and 6, shown in Eq. (8), interact with the first interface. Wave 6 represents a perturbation that travels through the second layer, advancing towards the first interface.

The amplitudes of the four waves shown in the previous equation depend on velocities and densities corresponding to the first two layers. Their phase (arrival time) depends on velocities and thicknesses associated with the first two layers [11]. We deduce from these equations that any change in the physical properties of one or various layers can affect the amplitudes and arrival times of deconvolved waves. This is discussed in detail in the following section.

The presence of up-going waves in Eqs. (7) and (8) denotes the existence of a virtual source placed at surface [9,28]. Since there is no real source, the boundary conditions associated with displacements differ from those fulfilled by the deconvolved wavefields [9]. As a consequence, the ascending arrivals defined in Eqs. (6) and (8) have negative arrival times. A comprehensive study of the properties of deconvolved fields can be found in Snieder et al. [9].

By deconvolving $U_3(h_1+h_2+c,\omega)$ with the displacement registered at the surface, we obtain

$$\frac{U_3(h_1+h_2+c,\omega)}{U_1(0,\omega)} = \frac{(k_1\beta_1^2\rho_1 + k_2\beta_2^2\rho_2)(k_2\beta_2^2\rho_2 + k_3\beta_3^2\rho_3)}{8k_2k_3\beta_2^2\beta_3^2\rho_2\rho_3}\left(e^{i(-k_1h_1-k_2h_2-k_3c)} + e^{i(k_1h_1+k_2h_2+k_3c)}\right) - \frac{(k_2\beta_2^2\rho_2 - k_1\beta_1^2\rho_1)(k_2\beta_2^2\rho_2 - k_3\beta_3^2\rho_3)}{8k_2k_3\beta_2^2\beta_3^2\rho_2\rho_3}\left(e^{i(k_1h_1-k_2h_2+k_3c)} + e^{i(-k_1h_1+k_2h_2-k_3c)}\right) - \frac{(k_1\beta_1^2\rho_1 + k_2\beta_2^2\rho_2)(k_2\beta_2^2\rho_2 - k_3\beta_3^2\rho_3)}{8k_2k_3\beta_2^2\beta_3^2\rho_2\rho_3}\left(e^{i(k_1h_1+k_2h_2-k_3c)} + e^{i(-k_1h_1-k_2h_2+k_3c)}\right)$$

$$+\frac{(k_2\beta_2^2\rho_2-k_1\beta_1^2\rho_1)(k_2\beta_2^2\rho_2+k_3\beta_3^2\rho_3)}{8k_2k_3\beta_2^2\beta_3^2\rho_2\rho_3}(e^{i(-k_1h_1+k_2h_2+k_3c)}+e^{i(k_1h_1-k_2h_2-k_3c)}) \tag{9}$$

Assuming for the moment that there is no attenuation and applying the inverse Fourier transform to the previous equation gives

$$\begin{aligned}\frac{u_3(h_1+h_2+c,t)}{u_1(0,t)} &= \frac{1}{2T_1T_2}\left[\overbrace{\delta\left(t+\frac{h_1}{\beta_1}+\frac{h_2}{\beta_2}+\frac{c}{\beta_3}\right)}^{7}+\overbrace{\delta\left(t-\frac{h_1}{\beta_1}-\frac{h_2}{\beta_2}-\frac{c}{\beta_3}\right)}^{8}\right]\\ &+\frac{R_2}{2T_1T_2}\left[\overbrace{\delta\left(t+\frac{h_1}{\beta_1}+\frac{h_2}{\beta_2}-\frac{c}{\beta_3}\right)}^{9}+\overbrace{\delta\left(t-\frac{h_1}{\beta_1}-\frac{h_2}{\beta_2}+\frac{c}{\beta_3}\right)}^{10}\right]\\ &+\frac{R_1R_2}{2T_1T_2}\left[\overbrace{\delta\left(t+\frac{h_1}{\beta_1}-\frac{h_2}{\beta_2}+\frac{c}{\beta_3}\right)}^{11}+\overbrace{\delta\left(t-\frac{h_1}{\beta_1}+\frac{h_2}{\beta_2}-\frac{c}{\beta_3}\right)}^{12}\right]\\ &+\frac{R_1}{2T_1T_2}\left[\overbrace{\delta\left(t+\frac{h_1}{\beta_1}-\frac{h_2}{\beta_2}-\frac{c}{\beta_3}\right)}^{13}+\overbrace{\delta\left(t-\frac{h_1}{\beta_1}+\frac{h_2}{\beta_2}+\frac{c}{\beta_3}\right)}^{14}\right],\end{aligned} \tag{10}$$

where $R_2=(\beta_3\rho_3-\beta_2\rho_2)/(\beta_3\rho_3+\beta_2\rho_2)$ and $T_2=(2\beta_3\rho_3)/(\beta_3\rho_3+\beta_2\rho_2)$. Eq. (10) allows us to identify the main features of the deconvolved wavefields in layered media. Based on Eq. (10), we can assert the following: the amplitudes of arrivals 9, 10, 11, 12, 13, and 14 are smaller than the amplitudes of waves 7 and 8. The arguments of waves 7, 10, 11, and 14 denote motion towards the second interface, whereas waves 8, 9, 12, and 13 move away from this interface. As in Eq. (8), the amplitudes and traveltimes of the deconvolved arrivals defined in the previous equation depend on the physical properties of the layered medium. Given that estimates of soil characteristic periods are relevant in seismic engineering, expressions such as Eqs. (6), (8), and (10) can be used to interpret deconvolved seismic records [11]. In conjunction with seismic events recorded in boreholes, theoretical deconvolutions (like Eqs. (6), (8), and (10)) can be used to identify interfaces (possibly significant for micro-zonification purposes) situated at depths smaller than the depth of the basement [11]. From Eqs. (6), (8), and (10), it is possible to see that the number of arrivals N detected in the deconvolved traces can be related to the number of the layer as follows: $N=2^l$, where l denotes the number of the layer [11]. Deconvolving the displacement field detected in layer M (where $M\geq 2$) with the corresponding motion detected at the surface produces

$$\begin{aligned}\frac{u_M\left(\sum_{n=1}^{M-1}h_n+w,t\right)}{u_1(0,t)} &= \frac{1}{2^M}\prod_{n=1}^{M-1}\left(\frac{\beta_n\rho_n}{\beta_{n+1}\rho_{n+1}}+1\right)\left[\overbrace{\delta\left(t+\sum_{n=1}^{M-1}\frac{h_n}{\beta_n}+\frac{w}{\beta_M}\right)}^{A}\right.\\ &\left.+\overbrace{\delta\left(t-\sum_{n=1}^{M-1}\frac{h_n}{\beta_n}-\frac{w}{\beta_M}\right)}^{D}\right]+\frac{1}{2^M}\prod_{n=1}^{M-1}\left((-1)^{n+1}\frac{\beta_n\rho_n}{\beta_{n+1}\rho_{n+1}}+1\right)\\ &\left[\overbrace{\delta\left(t+\sum_{n=1}^{M-1}\frac{h_n}{\beta_n}-\frac{w}{\beta_M}\right)}^{PR_1}+\overbrace{\delta\left(t-\sum_{n=1}^{M-1}\frac{h_n}{\beta_n}+\frac{w}{\beta_M}\right)}^{PR_2}\right]+\ldots\end{aligned} \tag{11}$$

where w represents the distance between the receiver deployed in layer M and the upper limit of this layer; A and D denote the main ascending and descending waves, respectively (the expressions for A and D include waves 3, 4, 7, and 8 as defined in Eqs. (8) and (10)); PR_1 and PR_2 define *pseudo reflections* (the expressions for these *pseudo reflections* include waves 5, 6, 9, and 10 as defined in Eqs. (8) and (10)). Eq. (11) does not include the rest of the *pseudo reflections*; if it did, this expression would be excessively complex, as the total number of arrivals corresponding to layer M is 2^M. To obtain Eqs. (6), (8), and (10), we assume no attenuation and then apply the inverse Fourier transform to Eqs. (5), (7), and (9). The expressions we obtain in the time domain when we consider attenuation are slightly more complicated than Eqs. (6), (8), and (10). The deconvolutions expressed in the time domain that include attenuation contain convolutions which are defined in terms of delta and exponential functions. The delta functions that appear in these expressions are exactly the same delta functions that are shown in Eqs. (6), (8), and (10), which implies that the traveltimes are not affected by attenuation [11]. It turns out that traveltimes are affected by attenuation, but, in most of the cases, it is assumed that the influence of attenuation on traveltimes is negligible. A more detailed discussion about the exponential functions that appear in the time domain convolutions (which include attenuation) is presented in the Appendix A.

We can interpret the waves denoted by the thin gray arrows shown in Fig. 4 in a qualitatively fashion using arrivals 5, 6, 9–14, PR_1, and PR_2 (at the end of this section, we interpret these waves considering attenuation). For shear waves, one of the most important velocity contrasts shown in Fig. 2 is the one associated with the interface located at 55 m of depth. At this depth, there is an important jump in terms of physical properties. As can be seen in the shear wave velocity profile, it is not clear below 13.5 m (at this depth there is another important velocity contrast) whether there is only one layer of basalt with some degree of erosion, or several layers of basalt that correspond to different episodes of volcanism. The shear wave velocity increases with depth (from 13.5 m–55 m). After 55 m, the shear wave velocity remains constant at 2800 m/s. Therefore, we can conclude that the *pseudo reflections*, denoted by thin gray arrows in Fig. 4, are produced by the transition zone that separates the sand sediments from solid basalt (with velocity of 2800 m/s).

For the station SMNH01, we can also detect interfaces located between the surface and 100 m of depth by measuring the amplitudes of deconvolved waves. In Fig. 4, the amplitudes of the main ascending waves denoted by the thick blue upward-pointing arrow are smaller than the amplitudes of the respective band-limited Dirac delta functions observed in the deconvolved traces associated with the receiver situated at the surface. We obtain each band-limited Dirac delta function by deconvolving the corresponding motion recorded at surface with itself. The amplitudes of these functions are close to one, as we include a "water-level" parameter in the deconvolution process (see Eq. (1)). To set the maximum amplitude of the deconvolved traces equal to one for each seismic event, we normalize all of the amplitudes of the deconvolved waves with respect to the maximum amplitude observed in the deconvolved trace corresponding to the surface. Note that in Fig. 4 the amplitudes of the main ascending waves (denoted by the thick blue upward-pointing arrow) are approximately seven times smaller than the amplitudes of the respective band-limited Dirac delta functions. In order to understand the influence of scattering in this amplitude behavior, we substitute both the shear wave velocities and the densities, shown in Fig. 2, in the amplitude of wave A defined in Eq. (11). From this calculation, we obtain an amplitude equal to 0.18, which approximately corresponds to the amplitudes associated with the main ascending waves (denoted by the thick blue upward-pointing arrow) registered in 1999 (see Fig. 4). It is

necessary to emphasize that this amplitude value does not account for attenuation, however from this value, it is possible to infer that there are at least four interfaces (detectable using seismic data) situated between the surface and the sensor deployed at 100 m (Fig. 2 shows the location of these interfaces).

In Fig. 4, the arrival time t of the main ascending and descending waves is given by $|t|=0.85$ s (measured from zero time to the time defined by the peak of each of one of these waves), whereas the arrival time that we obtain by substituting both the shear wave velocities and thicknesses, as shown in Fig. 2, in Eq. (11) gives 0.1 s, differing from the deconvolved arrival time. The absolute value of the arrival time corresponding to the *pseudo reflections* denoted by the thin gray arrows in Fig. 4 is equal to 0.3 s. In this figure, we can see that the amplitudes of these *pseudo reflections* are, in most of the cases, not negligible. In fact, in some cases, these amplitudes are comparable with the amplitudes of the main ascending waves (indicated in Fig. 4 by the thick blue upward-pointing arrow).

In order to study the behavior of the deconvolved fields in the presence of attenuation, we generate synthetic data using a model constituted by three layers overlying a half-space. We utilize the physical parameters shown in Fig. 2 as a reference. In our model, we add the layer number four, illustrated in Fig. 2, to the half-space, and set the shear wave velocity of the half-space equal to 2800 m/s. We modify some of the parameters shown in Fig. 2 to fit the deconvolved traces corresponding to the seismic event detected on 21/08/1999, see Fig. 7. In particular, we modify the physical parameters of the first layer. In order to include attenuation in the equations that govern the displacement fields, we employ a simplified hysteretic Kelvin's model. In this model, the wavenumber k is related to the quality factor Q through the following expression: $k=(\omega/\beta)(1-i/(2Q))$ [25]. To generate synthetic seismograms, we convolve the equations that govern displacement fields with the Fourier transform of a Ricker pulse with a dominant frequency of 5.9 Hz, using the FFT. Subsequently, we apply an IFFT to the convolved traces to transform these traces to the time domain. The synthetic deconvolved traces are shown in Fig. 7. Based on the synthetic data shown in Fig. 7 and other examples that we generated (which are not presented in this work), we can establish the following: (a) for values of $Q_1<15$ (quality factor of the first layer), the latest descending arrival (indicated with the thick green downward-pointing arrow) always develops a low amplitude, these modeling results explain the significant amplitude decay observed in the deconvolved arrivals denoted by the thick green downward-pointing arrow shown in Fig. 4; (b) the amplitudes of the *pseudo reflections* are governed by the individual values of ρ_1, β_1, and Q_1; (c) the amplitudes of the main ascending arrivals are smaller than those of the corresponding band limited Dirac delta functions, revealing the presence of the interfaces that separate the first layer from the half-space; (d) the amplitudes of the main ascending and descending waves are controlled by the individual values of ρ_1, β_1, and Q_1. From the synthetic experiments, we can also establish that the variability in terms of amplitudes observed in Fig. 4 indicates changes in physical properties. There is also variability in terms of amplitudes and traveltimes of the band-limited Dirac delta functions observed in the deconvolved traces that correspond to the surface (see Figs. 4 and 7), which also denote changes in the subsurface [29]. In the next section, we explain in greater detail the propagation of small velocity and density changes through amplitudes and arrival times of deconvolved waves.

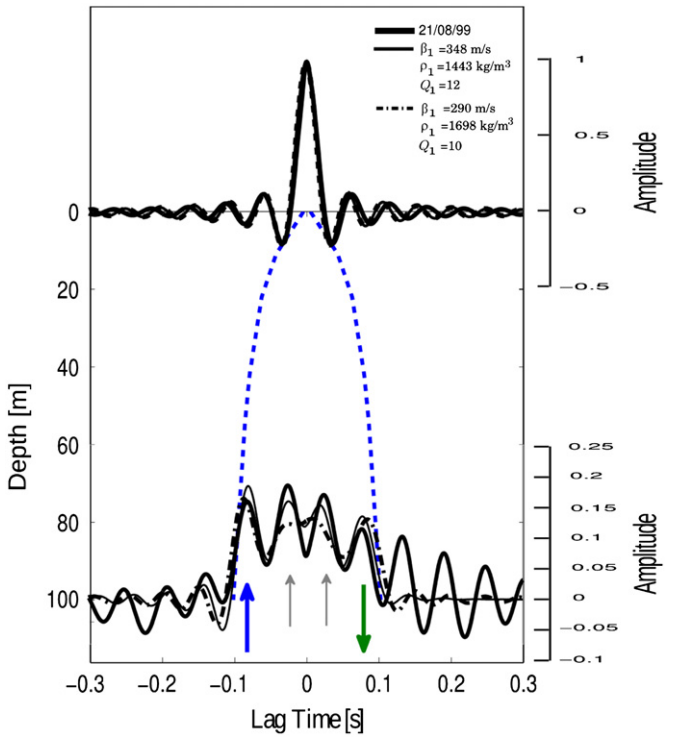

Fig. 7. Synthetic deconvolutions and deconvolved traces corresponding to the seismic event detected on 21/08/99 (see Table 1).

6. Propagation of small velocity and density changes (time-lapse variations) through amplitudes and arrival times of deconvolved waves

In this section, we introduce and describe the expressions that relate changes in near-surface physical properties (velocity and density) to variations in the amplitudes and arrival times of deconvolved waves in order to illustrate that it is possible to detect small time-lapse changes in near-surface properties using deconvolution. For the examples presented in this section, we do not consider attenuation and assume the signal-to-noise ratio to be optimal. Here, we consider the purely elastic case because this can be used as a case of reference.

6.1. Amplitude changes

We can identify the impedance ratio $I=(\rho_1\beta_1)/(\rho_2\beta_2)$ from the amplitude of the main ascending wave 3 shown in Eq. (8), defined below:

$$\frac{1}{4}\left(1+\frac{\rho_1\beta_1}{\rho_2\beta_2}\right). \tag{12}$$

Assuming that the second layer consists of soft material and that this contains fluids (this case may be useful for microseismic purposes), then it may be possible that this layer may experience compaction when subjected to earthquakes. If this is the case, the velocity of this layer should increase, and the density of the layer should decrease (due to the possible decrement in the amount of fluids). Thus, we can express the change in $I=(\rho_1\beta_1)/(\rho_2\beta_2)$ due to changes in velocity β_2 and density ρ_2 as

$$\delta I=\frac{\partial I}{\partial\beta_2}\delta\beta_2+\frac{\partial I}{\partial\rho_2}\delta\rho_2 \tag{13}$$

where δ stands for small changes. Performing the derivatives and

simplifying yields

$$\frac{\delta I}{I} = -\frac{\delta\beta_2}{\beta_2} - \frac{\delta\rho_2}{\rho_2} \tag{14}$$

This equation establishes that if, for instance, $\delta\beta_2/\beta_2 > 0$, $\delta\rho_2/\rho_2 < 0$, and $|\delta\beta_2/\beta_2| > |\delta\rho_2/\rho_2|$, $\delta I/I < 0$. Thus, after compaction and considering that the product $\rho_2\beta_2$ increases, we should expect to see ascending waves with smaller amplitudes in the deconvolved traces corresponding to receivers placed in the second layer. On the other hand, after compaction of the second layer, the amplitude of the main ascending arrival (wave 8 shown in Eq. (10)) observed in traces corresponding to detectors placed in the half-space should be either smaller or greater than the original amplitude. Evidently, it depends on the impedance ratios. If in the second layer ρ_2 increases (which can be due to an increment in fluids) and β_2 remains constant, the amplitudes of ascending waves observed in the deconvolved traces corresponding to receivers situated in the second layer should be smaller than the original amplitudes (as in the case described above). For receivers deployed in the half-space, the amplitude of the main ascending arrival should be either smaller or greater than the unperturbed one. Again, it depends on the impedance contrasts. The cumulative nature of the changes in velocity and density denoted by Eq. (14) may increase the possibility of recognizing small time-lapse changes in near-surface properties by measuring variations in the amplitudes of deconvolved events. Although, it is also possible that the sum of the changes as expressed in Eq. (14) may be equal to zero.

For a layered medium, such as that illustrated in Fig. 5, the amplitude of the main ascending wave detected in layer M (where $M \geq 2$) is given by (see Eq. (11))

$$\frac{1}{2^M}\prod_{n=1}^{M-1}\left(\frac{\beta_n\rho_n}{\beta_{n+1}\rho_{n+1}}+1\right) \tag{15}$$

If, in the layered medium illustrated in Fig. 5, the product $\rho_1\beta_1$ increases, the amplitude of the main ascending wave observed in deconvolved traces corresponding to receivers placed in any layer (with the exception of the first layer) and in the half-space should be greater than the original amplitude (before the change). If two or more layers experience changes, the behavior of the deconvolved amplitudes detected in layer M becomes more complicated due to the combined effects of multiple impedance ratios. The structure of Eq. (15) implies that small time-lapse changes in densities and velocities can be detected by measuring the deconvolved amplitude associated with the first deconvolved arrival, the main ascending arrival, recorded by the deepest receiver.

Above, we described cases where changes in physical properties of layers occur in the context of "linear behavior". The term "linear behavior" stands for the behavior of the materials subjected to compaction or expansion, which follow the rules of logic and common sense. However, it is perfectly valid that, even when the density of the first layer ρ_1 remains constant (or it may have increased due to the presence of water originated by precipitation, for instance), the velocity β_1 may still experience reduction during or immediately after the movement caused by small earthquakes. This type of behavior may arise in the presence of a nonlinear process called incipient liquefaction [30,31]. Thus, in the presence of incipient liquefaction, the amplitudes of the main ascending wave measured in traces corresponding to receivers deployed below the first layer may be smaller than the original amplitudes (before liquefaction).

6.2. Traveltime changes

We can perform a similar analysis using arrival times. In the case of the interval traveltime $T_2 = h_2/\beta_2$ that corresponds to wave 8 which is defined in Eq. (10), the expression that relates variations in this interval traveltime to changes in velocity and thickness is

$$\frac{\delta T_2}{T_2} = \frac{\delta\beta_2}{\beta_2} - \frac{\delta h_2}{h_2} \tag{16}$$

We can infer from the previous equation that if, for example, $\delta\beta_2/\beta_2 > 0$ and $\delta h_2/h_2 = 0$ (when a small earthquake happens, the thickness may experience very small changes, though pore pressure may increase substantially [30]), $\delta T_2/T_2 > 0$. Note that all the interval traveltimes of wave 8 have the same sign. Therefore, if all the physical parameters in the layered medium increase (or decrease) at the same time, the arrival time corresponding to wave 8 would be profoundly modified. In other words, the arrival time of wave 8 may facilitate the identification of changes in velocities. On the other hand, the signs of the interval traveltimes of waves 9–14 (defined in Eq. (10)) are not equal. This reduces the possibility of identifying changes in physical properties through these waves. Nevertheless, such waves may still be useful, especially for micro-zonification purposes [11] (as explained above, the arrivals denoted in Fig. 4 by thin gray arrows correspond to *pseudo reflections* produced by interfaces whose identification may be important for studies of earthquake engineering).

In the presence of nonlinear phenomena such as incipient liquefaction [30,31], the reduction of the shear wave velocity (and of the shear modulus) may give rise to an increment in the arrival time corresponding to the main ascending and descending waves [19,31].

7. Discussion

We have described exact expressions for deconvolutions corresponding to a 1D layered medium composed of homogeneous and purely isotropic layers under the incidence of shear waves. Unlike other methods, we derived the theoretical deconvolutions by using the explicit expression for the displacement field evaluated at the surface to deconvolve explicit expressions for displacement fields evaluated at different depths. It follows from the theoretical deconvolutions that the amplitudes and arrival times of deconvolved waves depend on the physical properties of the layered medium [11]. In fact, in the exact expressions, we can identify main ascending and descending waves [11,12] and *pseudo reflections* [11]. From the theoretical deconvolutions, it can be established that any change in at least one physical property of the layered medium may produce variations in the amplitudes and arrival times of deconvolved waves. In fact, even a small variation (e.g. 5%) in one of the shear velocities can produce visible changes, especially in the amplitudes of the main ascending and descending waves and in the *pseudo reflections*, clearly observable in the deconvolved trace corresponding to the deepest receiver. In addition, in the theoretical deconvolutions, we can include attenuation. The theoretical deconvolutions can be used to invert for the quality factor, considering frequency dependence [11]. A caveat for the application of this inversion is that *a priori* knowledge of the physical properties of the first layer is required.

We used theoretical deconvolutions to interpret deconvolved seismic events registered at the SMNH01 station of KiK-net. The lithology at this station consists of soil above 13.5 m; below this depth, there is only basalt. This station has two triaxial sensors, deployed at the surface and at 100 m of depth. The deconvolution of the motion registered at 100 m with respect to the movement recorded at surface produced, in all cases, four clearly visible wavelets, two with negative time and two more with positive time. From the theoretical deconvolutions, it was possible to

identify the main ascending (negative time) and descending (positive time) waves, which always corresponded to the deconvolved wavelets with the smallest and greatest arrival times, respectively. The other two wavelets were associated with *pseudo reflections,* although these two wavelets did not correspond exactly to two *pseudo reflections.* It is clear from the amplitude of the main ascending wave detected at 100 m that these wavelets represent the superposition of 30 *pseudo reflections*. In other words, these arrivals are interfering constructively. It may be possible to visualize all the *pseudo reflections* using another type of deconvolution [11] (although this also depends on the physical and geometrical properties of the subsurface). From the modeling results, we can establish that the changes in the amplitudes of the *pseudo reflections* identified in Fig. 4 are mainly governed by density, shear wave velocity, and quality factor of the first layer (ρ_1, β_1, and, Q_1, respectively). The first layer beneath the surface at station SMNH01 is composed of sand and gravel (see Fig. 2), which implies that changes in ρ_1 and β_1 can be related to the following factors: precipitation and recurrent seismic events [19,31], as well as incipient liquefaction [30,31]. From the numerical experiments and the interpretation of the deconvolved data, we can establish that the amplitudes and traveltimes of deconvolved waves shown in Fig. 4 denote changes due to precipitation and recurrent seismic events, we can also observe in this figure healing. The influence of precipitation and healing mechanisms on time-lapse changes is inferred from the increment in the amplitudes of the main ascending arrival (and of the *pseudo reflections*). This can be seen, for instance, when we compare the deconvolved amplitudes that correspond to the earthquake registered on 21/01/2010 with those of the quake recorded on 07/02/2011. On the other hand, the influence of incipient liquefaction can be inferred from the reduction in the shear wave velocity [19,31] (see Table 2), which also produces a decrement in deconvolved amplitudes (see Fig. 4).

8. Conclusions

None of the theories discussed in our work are new, the theoretical deconvolutions (shown in the main text) and the expression for the attenuation operator (shown in Appendix A) were previously derived by Trampert et al. [11], in their derivation, they used an *SH* wave propagator matrix. Based on our results, the following can be asserted:

- We observed *pseudo reflections* on the deconvolved traces obtained from the seismic data recorded at station SMNH01. These *pseudo reflections* revealed the presence of interfaces located between sand (β=290 m/s) and solid basalt (β=2800 m/s).
- The presence of four impedance contrasts situated between the surface and the sensor deployed at 100 m of depth was detected by measuring the amplitudes of the main ascending arrivals (denoted by the thick blue upward-pointing arrow in Fig. 4), such amplitudes were always smaller than the amplitudes of the corresponding band-limited Dirac delta functions observed in the deconvolved traces corresponding to the surface.
- The strong amplitude decay detected in some of the main descending waves (denoted by the thick green downward-pointing arrow in Fig. 4) was mainly due to intrinsic attenuation (see Fig. 7).
- The maximum change (always relative to the smallest value) measured in the effective shear wave velocity β (obtained through deconvolution) and the respective shear modulus μ corresponded to 3.8% and 7.8%, respectively. The variations in shear wave velocities detected at station SMNH01 are mainly due to the combined influence of precipitation and recurrent seismic events, which, in some cases, give rise to incipient liquefaction.
- We got quality factors Q for shear waves by fitting synthetic data to real deconvolutions (obtained from the earthquake registered on 21/08/99), such values were equal to 12 (for the layer of sand and gravel) and 200 (for the basalt).
- The good performance of the 1D layered-model is explained by Goto et al. [32], who demonstrated that, for the type of lithology displayed in Fig. 2, the oblique incidence case is identical to vertical incidence. This happens when the velocity increases with depth. To include the incident angle, the 1D case can be extended to the 3D case following the approach described in Trampert et al. [11].

Acknowledgments

The first author is grateful to the Consejo Nacional de Ciencia y Tecnología (CONACYT) for its financial support (project 128376). Partial support from DGAPA-UNAM and SIP-IPN under projects IN121709 and 20100473, respectively, is highly appreciated. We are grateful to the National Research Institute for Earth Science and Disaster prevention (NIED) for making the KiK-net data available. Andrés Pech thanks Kimberly Traube for her editorial support. We really appreciate the comments and suggestions of two anonymous reviewers.

Appendix A. Attenuation operator for layered media

In this appendix, we derive the attenuation operator for layered media using explicit expressions for the displacement fields. It can be clearly seen in Fig. 4 that the amplitudes of the main down-going wave (indicated by the thick green downward-pointing arrow) are consistently smaller than the amplitudes of the main up-going wave (indicated by the thick blue upward-pointing arrow). Since this asymmetry is mainly due to attenuation, we can estimate the quality factor by deconvolving these waves.

Deconvolving the Fourier transform of the main descending wave with that of the main ascending wave, and considering a layered medium such as that shown in Fig. 5, produces

$$D_1 = \left[e^{\left(\frac{-2a\omega i}{\beta_1}\right)}\right]\left[e^{\left(\frac{-2a\omega}{\beta_1}\gamma(Q_1)\right)}\right] \tag{A.1}$$

and

$$D_{p+1} = \left[e^{\left(\frac{-2s\omega i}{\beta_{p+1}}\right)}\prod_{q=1}^{p} e^{\left(\frac{-2h_q\omega i}{\beta_q}\right)}\right]\left[e^{\left(\frac{-2s\omega}{\beta_{p+1}}\gamma(Q_{p+1})\right)}\prod_{q=1}^{p} e^{\left(\frac{-2h_q\omega}{\beta_q}\gamma(Q_q)\right)}\right] \tag{A.2}$$

where $p=1, 2, \ldots, n$; D_1 results from the deconvolution of the main down-going and up-going waves recorded in the first layer; and D_{p+1} represents the deconvolution of the main descending and ascending waves detected in the $p+1$ layer. In these equations, a denotes the vertical distance between the position of a receiver installed in the first layer and the surface ($z=0$); s represents the vertical distance between the position of a receiver located in the $p+1$ layer and the upper limit of this layer; and $\gamma(Q)$ denotes the attenuation coefficient expressed as a function of the quality factor Q. Eqs. (A.1) and (A.2) both have two components, shown in brackets. The first component in both equations clearly represents a plane wave. These waves are defined in the time domain by $\delta(t+2a/\beta_1)$ and $\delta(t+\sum_{q=1}^{p}(2h_q)/(\beta_q)+(2s)/(\beta_{p+1}))$, respectively.

Thus, Eqs. (A.1) and (A.2) define convolutions of plane waves with functional forms that can be interpreted as attenuation operators. It is clear, then, that the attenuation operators corresponding to the first and $p+1$ layers are

$$\Lambda_1 = \left[e^{\left(\frac{-2a\omega}{\beta_1}\gamma(Q_1)\right)} \right] \tag{A.3}$$

and

$$\Lambda_{p+1} = \left[e^{\left(\frac{-2s\omega}{\beta_{p+1}}\gamma(Q_{p+1})\right)} \prod_{q=1}^{p} e^{\left(\frac{-2h_q\omega}{\beta_q}\gamma(Q_q)\right)} \right], \tag{A.4}$$

respectively.

The values of Q obtained through deconvolution, in principle, are mainly due to the combined influence of intrinsic attenuation and scattering. These two types of attenuation are difficult to separate. One possible way to split them is by developing an algorithm based on the structure exhibited by Eqs. (5), (7) and (9). From these equations, we can infer the contributions of scattering and intrinsic attenuation using the energy associated with the *pseudo reflections* and the ratio of amplitudes of the main ascending and descending waves, respectively [11].

It is worth emphasizing that Q values obtained using a constant Q model cannot fully explain the site effects. For example, if an earthquake shakes layers of softer, saturated material embedded within harder material, local fluid-pressure gradients may develop, giving rise to a wave-induced flow. To model this behavior, a better understanding of the Q variation as a function of frequency is needed. By using better models, it may be possible to display Q variations in space and frequency, which could then be utilized to study wave-induced flow [33] and viscosity [30]. Since the quality factors can be obtained from amplitude ratios of deconvolved waves, the amplitudes of these waves need to be clearly characterized [34,35].

References

[1] Lobkis OI, Weaver RL. On the emergence of the Green's function in the correlations of a diffuse field. Journal of the Acoustical Society of America 2001;110:3011–7.

[2] Campillo M, Paul A. Long-range correlations in the diffuse seismic coda. Science 2003;299:547–9.

[3] Snieder R, Sheiman J, Calvert R. Equivalence of the virtual-source method and wave-field deconvolution in seismic interferometry. Physical Review E 2006;73:066620.

[4] Sánchez-Sesma FJ, Campillo M. Retrieval of the green's function from cross correlation: the canonical elastic problem. Bulletin of the Seismological Society of America 2006;96:1182–91.

[5] Sánchez-Sesma FJ, Pérez-Ruiz JA, Campillo M, Luzón F. Elastodynamic 2D Green function retrieval from cross-correlation: canonical inclusion problem. Geophysical Research Letters 2006;33:L13305.

[6] Sánchez-Sesma FJ, Pérez-Ruiz JA, Luzón F, Campillo M, Rodríguez-Castellanos A. Diffuse fields *y* dynamic elasticity. Wave Motion 2008;45:641–54.

[7] Pérez-Ruiz JA, Luzón F, Sánchez-Sesma FJ. Retrieval of elastic Green's tensor near a cylindrical inhomogeneity from vector correlations. Communications in Computational Physics 2008;3:250–70.

[8] Vasconcelos I, Snieder R. Interferometry by deconvolution, part I—theory for acoustic waves and numerical examples. Geophysics 2008;73:S115–28.

[9] Snieder R, Miyazawa M, Slob E, Vasconcelos I, Wapenaar K. A comparison of strategies for seismic interferometry. Surveys in Geophysics 2009;30:503–23.

[10] Wapenaar K, van der Neut J, Ruigrok E, Draganov D, Hunziker J, Slob E, Thorbecke J, Snieder R. Seismic interferometry by crosscorrelation and by multidimensional deconvolution: a systematic comparison. Geophysical Journal International 2011;185:1335–64.

[11] Trampert J, Cara M, Frogneux M. *SH* propagator and Q_s estimates from borehole- and surface- recorded earthquake data. Geophysical Journal International 1993;112:290–9.

[12] Mehta K, Snieder R, Graizer V. Downhole receiver function: a case study. Bulletin of the Seismological Society of America 2007;97:1396–403.

[13] Sawazaki K, Sato H, Nakahara H, Nishimura T. Time-lapse changes of seismic velocity in the shallow ground caused by strong ground motion shock of the 2000 western-Tottori earthquake, Japan, as revealed from coda deconvolution analysis. Bulletin of the Seismological Society of America 2009;99:352–66.

[14] Rubinstein JL, Beroza GC. Evidence for widespread nonlinear strong ground motion in the Mw 6.9 Loma Prieta earthquake. Bulletin of the Seismological Society of America 2004;94:1595–608.

[15] Rubinstein JL, Beroza GC. Depth constrains on nonlinear strong ground motion from the 2004 Parkfield earthquake, evidence for widespread nonlinear strong ground motion in the Mw 6.9 Loma Prieta earthquake. Geophysical Research Letters 2005;32:L14313.

[16] Yamada M, Mori J, Ohmi S. Temporal changes of subsurface velocities during strong shaking as seen from seismic interferometry. Journal of Geophysical Research 2010;115:B03302.

[17] Singh SK, Mena E, Castro R. Some aspects of the source characteristics and ground motion amplifications in and near Mexico city from acceleration data of the September 1985 Michoacan, Mexico earthquakes. Bulletin of the Seismological Society of America 1988;78:451–77.

[18] Okada Y, Kasahara K, Hori S, Obara K, Sekiguchi S, Fujiwara H, Yamamoto A. Recent progress of seismic observation networks in Japan—Hi-net, F-net, K-net and KiK-net. Earth Planets Space 2004;156:15–28.

[19] Nakata N, Snieder R. Estimating near surface shear-wave velocities in Japan by applying seismic interferometry to KiK-net data. Journal of Geophysical Research 2012;117:B01308.

[20] Langston CA. Structure under Mount Rainier, Washington, inferred from teleseimic body waves. Journal of Geophysical Research 1979;84:4749–62.

[21] Jongmans D, Demanet D, Horrent C, Campillo M, Sánchez-Sesma FJ. Dynamic soil parameters determination by geophysical prospecting in México City: implication for site effect modelling. Soil Dynamics and Earthquake Engineering 1996;15:549–59.

[22] Sánchez-Sesma FJ. Site effects on strong ground motion. Soil Dynamics and Earthquake Engineering 1987;6:124–32.

[23] Sánchez-Sesma FJ, Chávez-Pérez S, Suarez M, Bravo MA, Pérez-Rocha LE. The México earthquake of September 19, 1985—on the seismic response of the Valley of México. Earthquake Spectra 1988;4:569–89.

[24] Sánchez-Sesma FJ, Pérez-Rocha LE, Reinoso E. Ground motion in México City Valley during the april 25, 1989, Guerrero Earthquake. Tectonophysics 1993;218:127–40.

[25] Carcione JM. Wave Fields in Real Media Wave Propagation in Anisotropic, Anelastic, Porous and Electromagnetic Media. UK: Elsevier-Oxford; 2007.

[26] Backus MM. Water reverberations—their nature and elimination. Geophysics 1959;24:233–61.

[27] Şafak E. Wave-propagation formulation of seismic response of multistory buildings. Journal of Structural Engineering 1999;125:426–38.

[28] Bakulin A, Calvert R. The virtual source method: theory and case study. Geophysics 2006;71:SI139–50.

[29] Cárdenas-Soto M, Chávez-García FJ. Application of seismic interferometry to obtain the response of buildings and soil deposits subjected to strong motions. In: Proceedings of the XVI Mexican congress of earthquake engineering [in Spanish].

[30] Snieder R, van den Beukel A. The liquefaction cycle and the role of drainage in liquefaction. Granular Matter 2004;6:1–9.

[31] Nakata N, Snieder R. Near-surface weakening in Japan after the 2011 Tohoku-Oki earthquake. Geophysical Research Letters 2011;38:L17302.

[32] Goto H, Sawada S, Hirai T. Conserved quantity of elastic waves in multi-layered media: 2D *SH* case—Normalized Energy Density. Wave Motion 2011;48:602–12.

[33] Pride SR, Harris MH, Johnson DL, Mateeva A, Nihei KT, Nowack RL, Rector JW, Spetzler H, Wu R, Yamomoto T, Berryman JG, Fehler M. Permeability dependence of seismic amplitudes. The Leading Edge 2003;6:518–25.

[34] Safak E. Discrete-time analysis of seismic site amplification. Journal of Engineering Mechanics 1995;121:801–9.

[35] Snieder R, Şafak E. Extracting the building response using seismic interferometry: theory and application to the Millikan Library in Pasadena, California. Bulletin of the Seismological Society of America 2006;96:586–98.